processes

MDPI

Article

Mechanisms and Mitigation of Viscous Fingering in Immiscible Displacement: Insights from Flow Channeling and Capillary Effects in Porous Media

Xin Yang [1,2,*], Bo Kang [1,3], Qi Deng [1], Zhongrong Mi [1], Ce Duan [1], Weiguang Wang [3] and Yanbing Tang [2,*]

[1] Chengdu Northern Petroleum Exploration and Development Technology Co., Ltd., Chengdu 610000, China
[2] State Key Laboratory of Oil and Gas Reservoir Geology and Exploitation, Southwest Petroleum University, Chengdu 610500, China
[3] EBS Petroleum Co., Ltd., Baghdad 10001, Iraq
* Correspondence: xwllyang@163.com (X.Y.); yb_tang@foxmail.com (Y.T.)

Abstract

The investigation of fluid flow channeling and viscous fingering during immiscible two-phase displacement in subsurface porous media is crucial for optimizing CO_2 geological sequestration and improving hydrocarbon recovery. In this study, we develop a pore-scale numerical framework for unsteady state immiscible displacement based on a body-centered cubic percolation network, which explicitly captures the coupled effects of pore-scale heterogeneity, capillary number, and unfavorable viscosity ratio on flow channeling and viscous fingering. The simulations reveal that viscous fingering and flow channeling preferentially occur along overlapping high conductivity pathways that conform to the minimum energy dissipation principle. Along these preferential routes, the local balance between viscous and capillary forces governs the stability of the two-phase interface and gives rise to distinct patterns and intensities of viscous fingering in the invading phase. Building on these insights, we establish a theoretical framework that quantifies how the critical pore radius and capillary number control the onset and growth of interfacial instabilities during immiscible displacement. The model demonstrates that lowering the injection rate, and hence, the effective capillary number, suppresses viscous fingering, leading to more stable displacement fronts. These findings provide practical guidance for the design of injection schemes, helping to enhance oil and gas recovery and improve the storage efficiency and security of CO_2 geological sequestration projects.

Keywords: unsteady state immiscible displacement; heterogeneity; flow channeling; viscous fingering; critical radius

Check for updates

Academic Editors: Zhijie Wen, Jian Tao and Qingbang Meng

Received: 19 November 2025
Revised: 8 January 2026
Accepted: 14 January 2026
Published: 19 January 2026

Copyright: © 2026 by the authors. Licensee MDPI, Basel, Switzerland. This article is an open access article distributed under the terms and conditions of the Creative Commons Attribution (CC BY) license.

1. Introduction

Immiscible two-phase flow in porous media is ubiquitous in fields such as geophysics, petroleum engineering, and chemical engineering [1]. The unstable displacement process, particularly viscous fingering, represents a key research focus for these disciplines [2–5]. Research on viscous fingering is highly relevant for advancing underground carbon dioxide engineering, including the efficiency and safety optimization of CO_2 capture, utilization, and storage (CCUS) and geological sequestration operations [6,7]. Despite considerable research effort over the decades, the mechanisms underlying the formation of viscous fingering and effective strategies for its suppression remain poorly understood, particularly

under the dynamic conditions encountered in complex systems like oil production and geological sequestration [8].

During immiscible two-phase flow on the pore scale, viscous fingering emerges as a significant instability at the displacement interface. This phenomenon becomes particularly pronounced when the viscosity of the injected phase is much less than that of the resident fluid, combined with high displacement velocities or injection rates that correspond to a large capillary number (*Ca*) [9]. Additionally, the inherent stochastic heterogeneity of porous media amplifies the development and evolution of viscous fingering [1]. This dynamic instability produces asymmetric, irregular, and localized "finger-like" flow structures in the displacement process [10]. In practice, viscous fingering often has adverse effects on critical applications. For example, it can confine fluid flow to high-permeability zones in oil reservoirs, causing lower-permeability regions to be bypassed and leading to suboptimal resource recovery [11,12]. Similarly, in environmental remediation, such as groundwater cleanup, viscous fingering reduces the sweep efficiency of injected reagents, thereby hindering uniform contaminant removal [13].

Viscous fingering in immiscible two-phase flow is commonly characterized by (i) a highly unstable displacement interface; (ii) strong localization of flow into a limited number of preferential pathways; and (iii) a pronounced dependence on both pore-scale geometric heterogeneity and hydrodynamic imbalance (e.g., adverse mobility/viscosity contrast) [14]. A recurring observation across experimental visualization and pore-scale simulations is that fingers advance by exploiting the least-resistance routes of the porous matrix, which conceptually connects viscous fingering to the well-studied phenomenon of single-phase channeling in porous media [15]. In single-phase settings, channeling denotes the tendency of flow to concentrate along a subset of connected pores and throats that collectively minimize hydraulic resistance, often associated with high connectivity, locally larger conductance, or regions where energy dissipation is concentrated [16].

Building on this view, recent studies have reported that, under otherwise comparable conditions, the spatial footprints of viscous fingers frequently coincide with (or are "seeded" by) the dominant channeling backbones that would be selected in single-phase flow through the same pore network [16]. In immiscible displacement, this overlap is further reinforced by additional, phase-dependent resistances introduced by the presence of a moving interface and by the viscosity of the displaced phase: high-viscosity resident fluids amplify the pressure gradients required for invasion and strengthen the positive feedback between local permeability advantage and faster front propagation. This coupling between channeling-controlled pathway selection and interfacial destabilization ultimately yields the hallmark asymmetric, ramified finger-like patterns observed in viscous fingering [17]. Recent advances have been achieved using a combination of experimental, theoretical, and numerical approaches. Experimentally, Hele-Shaw cells are commonly employed to investigate viscous fingering by varying control parameters such as viscosity ratio, flow rate, and permeability gradients to study the evolution of interfaces and displacement patterns [8,18]. For example, studies have demonstrated that altering injection velocities or applying dynamic injection strategies can stabilize displacement fronts and improve interface uniformity [12]. Furthermore, modifying the geometry of pore structures significantly impacts the onset and evolution of viscous fingering [19]. From a theoretical perspective, analogies between viscous fingering and interfacial dynamics in fluid mechanics, such as diffusion-limited aggregation and flame propagation models, have offered insights into the complex balancing mechanisms between energy distribution and interfacial forces [5]. Numerically, significant progress has been achieved using dynamic pore network modeling, which visualizes non-uniform flow pathways and assesses the evolution of viscous fingering via parameters such as viscous forces, capillary forces, and pore anisotropy [16]. For

instance, dynamic percolation models have explained capillary trapping in oil and water systems and quantified the effects of flow architecture on displacement efficiency [20].

Nevertheless, mitigating viscous fingering remains a persistent challenge because suppression is governed by a coupled balance among viscous forces, capillary forces, and pore-scale heterogeneity, and therefore, cannot be reliably achieved by tuning a single operational variable. Existing studies have explored a range of control approaches from both the operational and the material/structural perspectives. On the operational side, lowering injection rate (i.e., reducing *Ca*) is widely recognized as a direct means to stabilize displacement fronts, although it is often constrained by field-scale productivity requirements and may not prevent preferential pathway selection in strongly heterogeneous media [18]. Related strategies include variable or pulsed injection and mobility-control schemes that target the growth of dominant fingers by altering the local pressure gradient and effective mobility ratio during displacement. On the fluid-property side, increasing the viscosity of the injected phase using polymers, foams, or other thickeners can reduce adverse mobility contrast and has been shown to delay finger initiation and promote more uniform sweep; however, the effectiveness is highly system-dependent and can be compromised by pore-scale trapping, dispersion, and degradation effects in complex porous structures. In parallel, structural regulation—such as introducing permeability or pore-size gradients and tailoring heterogeneity patterns—has been investigated to redistribute flow resistance and weaken the positive feedback between preferential pathways and interface advancement, thereby moderating fingering intensity.

Despite these advances, a major limitation of prior work is that suppression strategies are often evaluated empirically and remain difficult to generalize across porous media types and displacement conditions. In particular, the mechanistic link between single-phase flow channeling (the preferential selection of least-resistance pathways) and the subsequent emergence of two-phase interfacial instability under non-equilibrium displacement has not been quantitatively established [16]. As a result, current approaches still lack a robust predictive criterion that connects pore-scale connectivity and channeling tendencies to the onset and dominance of viscous fingering, which is essential for designing transferable, quantitatively grounded suppression strategies. The objective of this study is to systematically investigate the coupling effects between fluid flow channeling and viscous fingering through the construction of high-resolution pore network models of heterogeneous porous media combined with dynamic displacement simulations. This study seeks to quantitatively analyze the formation conditions of viscous fingering and develop effective suppression strategies. By integrating analyses of single-phase flow channeling with investigations into two-phase flow instability, this work aims to elucidate the relationships between the pathways involved in viscous fingering generation and the critical parameters governing fluid flow. This study proposes a unified critical-radius–capillary-number (*rc*-*Ca*) framework that quantitatively links pore-scale connectivity, viscous fingering, and macroscopic sweep efficiency in heterogeneous porous media. Building on this framework, we develop an *rc*-*Ca*-based predictive criterion to delineate the critical conditions for the transition from channeling-dominated to viscous-fingering-dominated displacement. To the best of our knowledge, such a unified *rc*-*Ca* description with quantitative predictive capability has not been reported previously. Ultimately, the proposed methods, including optimizing injection rates, adjusting viscous contrasts, and regulating pore structure gradients, aim to suppress viscous fingering effectively, thereby enhancing oil and gas recovery and improving the outcomes of CO_2 geological sequestration. Meanwhile, this study concurrently accounts for the synergistic effects of flow channeling and capillary forces at the pore scale in porous media and introduces corresponding quantitative evaluation

metrics, thereby addressing critical research gaps in the understanding of viscous fingering mechanisms and the coupled mechanisms between flow channeling and capillary effects.

2. Materials and Methods

2.1. Pore Network Modeling

Network modeling is widely used to numerically investigate microscopic transport mechanisms governed by pore-scale fluid dynamics and to upscale these processes to the continuum scale [21]. In such simulations, dissipative and entropy-generating phenomena (e.g., viscous flow, diffusion) are assumed to occur only in the network branches, while conservation laws (Kirchhoff equations) are applied at each node [15].

A body-centered cubic (BCC) pore network was generated following the numerical procedure of Li et al. [22]. Variability in the coordination number z was introduced by randomly removing a subset of pipes with probability 1-p, where $p = z/z_{max}$ and $z_{max} = 8$ is the maximum coordination number of the BCC network. For example, setting $z = 4$ by removing half of the connections modifies the network connectivity. In each model, the mean pore–throat length l was set to 300 μm, and the simulations employed a BCC structure with 29,449 nodes (a 25 × 25 × 25 grid). Pore size distribution heterogeneity was governed using independent stochastic parameters following a log-uniform distribution, characterized by a normalized standard deviation $\sigma/\langle r\rangle$ (here, 0.8 and 1.05). This metric directly reflects the breadth of pore sizes, which can be quantified in natural samples via 2D/3D imaging and other analytical methods (such as NMR, mercury intrusion, or digital image analysis) [23]. The pore radii within this work were specified so that all models maintained a consistent hydraulic radius (r_H), given by 2 times the pipe's volume-to-surface area ratio and set at 40 μm. The link between pipe radius limits ([r_{min}, r_{max}]), normal distribution width ($\sigma/\langle r\rangle$), and hydraulic radius (r_H) follows the relationship below [16]:

$$\sigma/\langle r\rangle = \sqrt{\frac{\ln(r_{max}/r_{min})(r_{max}+r_{min})}{2(r_{max}-r_{min})} - 1} \quad (1)$$

$$r_H = \frac{r_{max}+r_{min}}{2} \quad (2)$$

Since the flow channeling is strong for heterogeneous rocks, we set the range of z to 4~8 in this work. The details of the values of r_H, $\sigma/\langle r\rangle$, and [r_{min}, r_{max}] can be found in the work of Bernabé et al. [14].

2.2. Single-Phase Flow

Single-phase fluid flow within the network was simulated by calculating fluid pressures at each node and average fluid velocities through the system, utilizing the Kirchhoff equations. These equations were resolved using impermeable (no flow) boundary conditions, as described in [24], and the principal flow orientation was set horizontally. For any tube linking nodes i and j, the volumetric flux q_{ij} without an interface in the tube follows Poiseuille's law, expressed as follows:

$$q_{ij} = g_{ij}\Delta p_{ij} = \frac{\pi r_{ij}^4}{8 l_{ij}\mu}(p_i - p_j) \quad (3)$$

Here, p_i and p_j represent the pressures at nodes i and j, while r_{ij} and l_{ij} denote the tube's radius and length, respectively. The fluid viscosity within each tube is given by μ. At each node, the pressures for both injected and displaced phases are consistent, and the net volumetric flux is zero ($\Sigma_j q_{ij} = 0$). This condition leads to a set of linear equations for

single-phase flow throughout the network, according to the Kirchhoff law. The resulting pressure distribution, p_i, can be determined using the preconditioned conjugate gradient (PCG) algorithm [25]. After computing nodal pressures, the overall volumetric flow rate (q, in m^3/s) across the network is found, and the permeability (k) of the model is evaluated via Darcy's law, with $k = q\mu L/(A\Delta p)$. Here, A is the cross-sectional area of the network (m^2), L is the network length (m), and Δp is the applied pressure drop across the network (Pa).

2.3. Unsteady State Immiscible Two-Phase Displacement

The assumptions for multiphase immiscible displacement are summarized as follows: (1) All fluids are assumed to be fully contained within the throats and nodes of the pore-network model (PNM), while all pressure drops occur only in the throats between nodes. (2) Only one two-phase fluid interface is allowed within a single throat. (3) For two immiscible and incompressible fluids, the displacing fluid is treated as the non-wetting phase. (4) The capillary pressure at the fluid–fluid interface at a throat entrance is inversely proportional to the throat radius. (5) Fluid fluxes are calculated using the Poiseuille equation. (6) Displacement within the pore space is assumed to proceed via piston-like displacement.

At the beginning of the simulation, the model is filled with the wetting phase fluid (viscosity μ_w). The injection of the non-wetting phase fluid (viscosity μ_{nw}) is then carried out at a constant flow rate through the inlet, representing the drainage scenario. The capillary pressure (p_c) that develops at the interface between the wetting and non-wetting fluids within tube i, which links to node j (that is, at the meniscus of the two immiscible phases), can be determined using the Young–Laplace equation as follows:

$$p_{cij} = -\frac{2\gamma \cos\theta}{r_{ij}} \tag{4}$$

Here, γ denotes the interfacial tension (in N/m), θ represents the contact angle (assigned a value of 100°), and r_{ij} specifies the tube's radius. The volumetric flow rate q_{ij} between pores i and j is calculated based on the Washburn model for capillary-driven flow [26,27]. For a cylindrical tube that contains a single two-phase meniscus, the volumetric flow rate q_{ij} can be described by the modified Poiseuille equation [28]:

$$q_{ij} = \frac{\pi r_{ij}^4}{8 l_{ij} \mu_{eff}} \left(\Delta p_{ij} - p_{cij}\right) \tag{5}$$

Here, μ_{eff} represents the effective viscosity (Pa·s) of the two-phase fluids coexisting within the tube. For tubes containing a single meniscus, μ_{eff} is calculated as $\mu_{eff} = \mu_{nw} \times x_{ij} + \mu_w \times (1 - x_{ij})$, where x_{ij} is the dimensionless position of the meniscus within the conduit ($0 \leq x_{ij} \leq 1$). For tubes containing only a single phase, $\mu_{eff} = \mu_{nw}$ or μ_w, and the capillary pressure $p_c = 0$, simplifying Equation 5 to the Hagen–Poiseuille equation (Equation 3). For low-Reynolds-number viscous flow in pore throats, the pressure drop is dominated by viscous dissipation; when the two phases occupy a pore throat in series (separated by a meniscus) and the local interfacial effects can be effectively represented by the "fractional lengths of each phase segment," length-weighted (equivalently, an arithmetic-type mixture) effective viscosity can be constructed for the pore throat and used in a Poiseuille-type relation. We also emphasize its limitations: if significant film flow exists, if nonlocal dissipation induced by dynamic contact angles occurs, or if additional interfacial resistance near the meniscus is non-negligible, this effective viscosity may deviate from the true hydraulic resistance.

In the pore network model, the two-phase fluids are assumed to be compressible. The flow between the central pore i of each control volume (composed of pore i and its

adjacent four throat segments) and neighboring pores j (where j = 1 to N, N is the total node number of the model) is governed by the principles of unsteady state immiscible two-phase displacement [12]:

$$-\sum_{j=1,\, j\neq i}^{N} \frac{\pi r_{ij}^4}{8 l_{ij} \mu_{eff}} \left(\Delta p_{ij} - p_{cij}\right) = V_p C_{\rho eff} \frac{\Delta p_i}{\Delta t} \quad (6)$$

Here, V_p represents the control volume centered at pore i, and $\Delta p_i/\Delta t$ denotes the temporal change in the average pressure of the control volume. $C_{\rho eff}$ is the effective compressibility of the mixed fluid, which depends on the fluid properties and is influenced by external conditions such as pressure and temperature. For the oil and water system studied in this work, $C_{\rho eff}$ is set to 1×10^{-10} Pa^{-1}. By combining Equation (6) with Kirchhoff's law, a set of nonlinear equations is established at each network node to solve for the nodal pressures p_i. During the simulation, the inlet and outlet pressures are kept constant over each time step Δt. To efficiently solve the large-scale sparse linear systems arising from repeated pressure-field calculations, an algebraic multigrid preconditioned conjugate gradient (AMG–CG) solver is employed [29]. During the displacement simulation, when a pore node becomes fully occupied by the injected fluid, the locations of all residual interfaces (menisci) in the adjoining tubes are documented. The network's pressure distribution is then updated, as well as the saturation values, allowing the simulation to advance to the following time step. Throughout the process, the overall injection or flow rate Q remains fixed. The overall workflow consists of initialization, pressure-field solution, interface/phase-state update, time advancement or event-driven advancement, convergence check, and output of flow rate and pressure. When the flow-rate fraction of the displacing fluid exceeds 99.99% of the total flow rate, the termination criterion is deemed satisfied, and the simulation is terminated. The pressure field is formulated as a sparse linear system based on mass conservation and solved via LU decomposition. Interface advancement follows an event-driven invasion–occupation update rule [16]. Convergence is declared when the residual falls below 10^{-6}.

At the pore scale, two key dimensionless parameters are often used to describe the displacement process: the capillary number (Ca) and the viscosity ratio ($M = \mu_w/\mu_{nw}$) [26]. The capillary number is calculated as $Ca = Q\mu_{nw}/(A\gamma)$, where A is the cross-sectional area of the pore network, and the interfacial tension γ is taken as 20 mN/m. In this research, the capillary number varies between 10^{-6} and 10^{-3}, covering a range typical for water/oil or supercritical CO_2/water systems at the laboratory scale, with the viscosity ratio set to an unfavorable value (M = 100) [12]. The non-wetting phase saturation (S_{nw}) at breakthrough is used as a metric to evaluate displacement sweep efficiency.

2.4. Model Validation

To investigate fluid behavior during the drainage process, a homogeneous network model was employed in this study (a thin-plate-like 1 cm × 3 cm three-dimensional BCC network with 38,600 nodes, $\sigma/\langle r\rangle$ = 0.3, and coordination number z = 4.5; the hydraulic radius r_H = 20 μm, with a porosity and permeability of 9.2% and 481.3 mD, respectively), as illustrated in Figure 1. The model was used to analyze the impact of uniform pore distribution on fluid flow characteristics. Figure 1a presents the pore throat size distribution (r_i-field distribution) under uniform radius distribution ($\sigma/\langle r\rangle$ = 0.3) conditions. The normalized flow flux distribution (q_i, q_i-field) and the normalized mean flow velocity distribution (v_i, v_i-field) also show how homogeneous pore networks affect single-phase fluid flow. For analysis purposes, the volumetric flow rate (q_i) and mean flow velocity (v_i) for all tubes were normalized by the maximum flow rate (q_{max}) and maximum velocity (v_{max}), using the normalization formulas $|q_i/q_{max}|$ and $|v_i/v_{max}|$, respectively.

Simulation results indicate that q_i and v_i exhibit a proportional relationship, expressed as $v_i \propto q_i / r_i^2$.

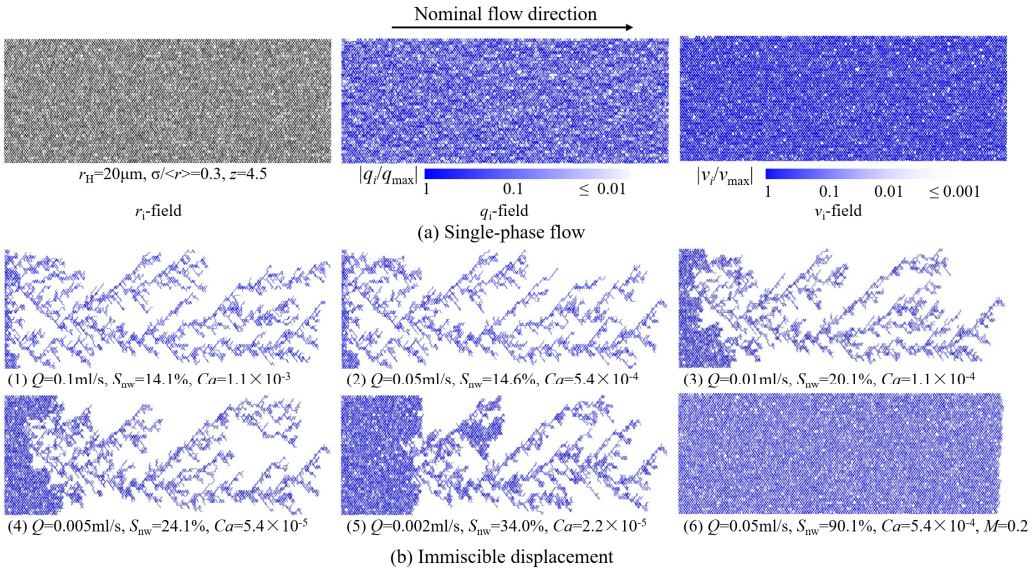


Figure 1. (**a**) Simulation results in the homogeneous network (1 cm × 3 cm three-dimensional BCC network with 38,600 nodes), with σ/<*r*> = 0.3 and *z* = 4.5, for the pore throat size distribution (r_i-field, black line is pore throat pipe), the normalized flow flux distribution (q_i-field) and the normalized mean flow rate distribution (v_i-field) of single-phase flow are presented in (**a**). (**b**) Viscous fingering with different capillary numbers, *Ca*, is shown in (1)~(5). The stable, compact displacement with *M* = 0.2 is presented in (6); S_{nw} is the saturation of the injected non-wetting phase at breakthrough.

The results further demonstrate that, in a homogeneous network (or rock), the flow velocity distribution across the entire pore space is approximately uniform. The pore space distribution of homogeneous rocks can, to some extent, be compared to the flow characteristics observed in Hele-Shaw cells. Previous studies on fluid–fluid displacement within Hele-Shaw cells have shown that, for unfavorable viscosity ratios (*M* > 1), higher injection rates (*Q*) lead to more pronounced viscous fingering phenomena [8,30]. The simulation results in this study (Figure 1b) reveal a similar linear relationship in homogeneous porous media. This finding is consistent with the experimental and numerical results reported by Zhao et al. [26], Regaieg et al. [3], and Lenormand et al. [9]. For unfavorable viscosity ratios (*M* > 1), a mixed mode of capillary fingering and viscous fingering emerges in the displacement process (illustrated as processes (1) to (5) in Figure 1b). In contrast, under favorable viscosity ratio conditions (*M* = 0.2), the displacement process transitions to stable and compact displacement, as shown in stage (6) of Figure 1b. These results demonstrate that the dynamic network model developed in this study successfully reproduces displacement patterns that have been observed in previous experimental and numerical studies.

3. Results and Discussion

3.1. The Relationship Between Flow Channeling and Viscous Fingering

Numerous investigations have indicated that flow channeling can be observed in aquifers across various scales [31,32]. In this section, we constructed a heterogeneous network model (with parameters *z* = 4.5, σ/<*r*> = 0.8, and r_H = 40 μm; see Figure 2) to investigate the relationship between flow channeling and viscous fingering. For heterogeneous rocks with high σ/<*r*>, the q_i- and (energy dissipation) $q_i \Delta p_i$-fields (Figure 2a) appeared highly non-uniform. The porosity and permeability of this network model is 20.1% and 650.5 mD, respectively. Flow localization within limited pore spaces gives rise to

several preferential flow channels, which makes it challenging to accurately capture the underlying network connectivity. It has been found that viscous fingers formed by the injected non-wetting phase tend to advance along the high-q_i and high-$q_i\Delta p_i$ pathways. In general, the dynamics of unstable immiscible two-phase flow are governed by the competition between viscous and capillary forces. When the injection rate Q is relatively large (relatively high Ca), the viscous force mainly controls the displacement. The high-q_i and high-$q_i\Delta p_i$ flow channeling in single-phase flow seems to form the viscous fingering paths in immiscible displacement (see Figure 2a).

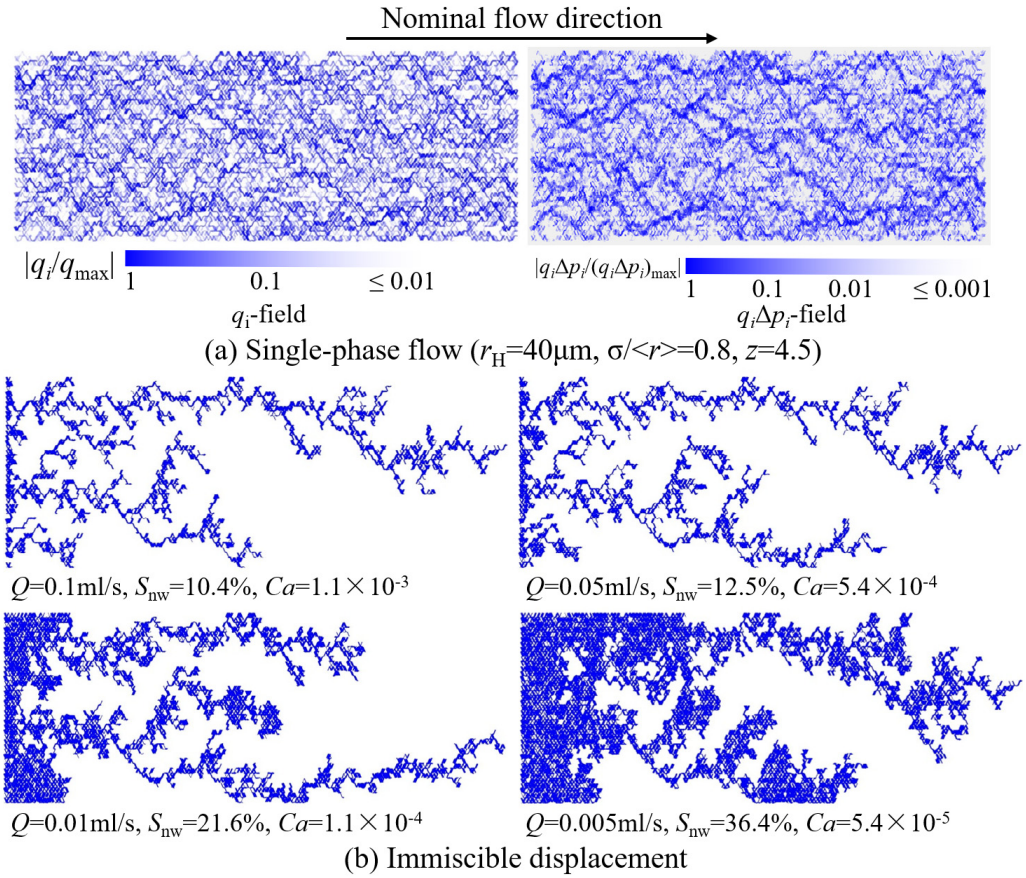


Figure 2. (**a**) Simulation results in the heterogeneous network (quasi two-dimensional BCC network with 38,600 nodes) with σ/<r> = 0.8 and z = 4.5. The normalized low flux distribution (q_i-field) and the normalized mean energy dissipation distribution ($q_i\Delta p_i$-field) of the single-phase flow are presented. (**b**) Viscous fingering is represented under different capillary numbers Ca; S_{nw} is the saturation of the injected non-wetting phase at breakthrough. The figure roughly illustrates that the viscous fingering crosses the pathways of the flow channeling.

During fluid flow through porous media, the fluid naturally selects pathways offering the least resistance between the inlet and outlet. Mathematically, this optimal route minimizes the value of $[\sum(1/r_{ij}^4)]$ across all possible paths. Algorithms such as Dijkstra's or the Top-K Shortest Path (KSP, with K = 1) [33] can be used to identify this physical flow path. In this study, two auxiliary nodes, U and D, were incorporated into the network: U connects to every upstream boundary node, while D connects to all downstream boundary nodes, both with zero distance assigned to these connections. Using Dijkstra's algorithm, the most efficient route from U to D is identified, and the smallest pipe radius along this path is defined as the critical radius, r_c (representing channeling path).

According to Figure 2b, it seems that the pathways of flow channeling and viscous fingering almost overlap. Here, Dijkstra's algorithm was also employed to analyze the flow

characteristic of viscous fingering. The critical radius r_{cw} (representing a viscous finger path) of the invasion water phase is defined as the lowest pipe radius of Dijkstra's viscous fingering path. Note that the viscous fingering grows with time and the front position of the viscous finger before breakthrough. The relations between flow channeling and the viscous finger can be quantificationally explained using r_{cw}/r_c.

The invasion percolation algorithm is applied to the network by continuously scanning the list of pipes—arranged from largest to smallest radius—until a pipe that is accessible, meaning it is connected to at least one already occupied node, is identified. During the one-face displacement, such as the invasion percolation process, once the invasion-phase breakthrough from the outlet, the capillary radius, corresponding to the invasion pressure, is defined as the critical radius r_c* (representing invasion-percolation capillary finger) of the capillary fingering. The values of r_c and r_c* for the same pore scale heterogeneity are given in Table 1. Note that r_c* is always larger than r_c.

Table 1. The values of r_c and r_c* for different pore scale heterogeneities.

σ/<r>	z	k/k_0	r_c/r_H	r_c^*/r_H
0.8	8	0.4328	0.9374	1.08
0.8	7.2	0.32	0.7485	1.01
0.8	6.4	0.2216	0.8846	0.9688
0.8	5.6	0.1274	0.6958	0.8525
0.8	4.8	0.067	0.5959	0.7512
0.8	4	0.0295	0.5249	0.6637
1.05	8	0.1742	0.921	0.9958
1.05	7.2	0.1099	0.7176	0.825
1.05	6.4	0.0672	0.6565	0.7562
1.05	5.6	0.0353	0.5572	0.6475
1.05	4.8	0.0167	0.4361	0.56
1.05	4	0.0051	0.4366	0.4812

The relatively high *Ca* ($Ca = 7 \times 10^{-3}$) displacement (water displacing oil) with the unfavorable viscosity ratio ($M = 100$) was performed in networks with different pore-scale heterogeneities to study the r_{cw}/r_c before breakthrough. The simulation results are plotted in Figure 3 (the distance x represents the location of the displacement front. When x reaches 100%, the displacement front reaches the outlet of the network. To differentiate flow channeling, viscous fingering, and capillary fingering in invasion percolation processes, the lines of r_c^*/r_c are also plotted in Figure 3. In Figure 3, it is observed that (1) the values of r_{cw}/r_c are less than r_c^*/r_c, showing that the flow pathways of viscous fingering and capillary fingering are different; (2) the values of r_{cw}/r_c are almost larger than 1 when $x < 50\%$, and the values of r_{cw}/r_c become closer to 1 when $x > 50\%$. Combined with Figures 2 and 3, this result indicates that viscous fingering mainly grows along the pathways of flow channeling. From the perspective of the coupling between viscosity ratio and capillary number, as the capillary number increases, viscous forces become dominant over capillary forces, making the interface more likely to break through early along high-permeability channels or large-pore pathways, thereby altering the initial position and growth path of the fingering.

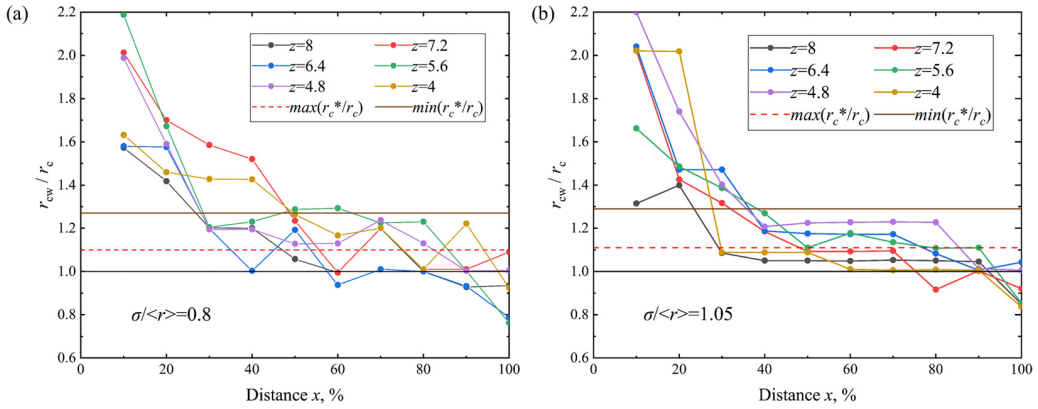


Figure 3. The simulated values of r_{cw}/r_c for different pore-scale heterogeneities with $Ca = 7 \times 10^{-3}$ and unfavorable viscosity ratio M ($M = 100$). The distance x represents the location of the displacement front. When x reaches 100%, the displacement front reaches the outlet of the network. The value of r_c^*/r_c is also plotted in the finger. The difference between r_c^*/r_c and r_{cw}/r_c indicates that the viscous fingering is more likely to flow along the pathways of flow channeling, but not the pathway of capillary fingering. (**a**) represents $\sigma/<r> = 0.8$, (**b**) represents $\sigma/<r> = 1.05$, and the solid black horizontal line in the figure indicates that the values of r_{cw} and r_c are identical.

3.2. Theoretical Model for Suppression of Viscous Fingering

Since the smallest pore throat radius r_c, located on the critical flow pathways, governs the viscous fingering under unfavorable viscosity ratios, reducing the injection rate can effectively control viscous fingering by increasing the relative capillary forces exerted by the smallest pore throats within the flow channeling pathways. Given that viscous fingering is unavoidable in displacements with unfavorable viscosity ratios, achieving dynamic equilibrium among the displacement pressure difference, viscous pressure drop, and capillary forces is essential to maximize sweep efficiency at breakthrough. Therefore, it is necessary to investigate optimization strategies for suppressing viscous fingering from the perspective of theoretical predictions. The equivalent capillary force, P_c, is expressed as follows:

$$P_c = \frac{2\gamma}{r_c} \tag{7}$$

where γ is the water and oil interfacial tension. According to Darcy's law, the displacement pressure difference ΔP is given by the following:

$$\Delta P = \frac{\mu_{eff}}{k} \cdot \frac{qL}{A} \tag{8}$$

where A and L represent the cross-sectional area and length of the network, respectively, k is the permeability, q is the flow rate, and μ_{eff} is the effective viscosity. When oil and water are macroscopically mixed within the porous medium, the effective viscosity μ_{eff} is computed as the geometric mean:

$$\mu_{eff} = \mu_w M^{1-S_w} \tag{9}$$

where S_w is the water saturation. Consequently, the displacement pressure difference ΔP can be rewritten as follows:

$$\Delta P = \Delta P_v + P_c \tag{10}$$

where ΔP_v is the viscous pressure loss. By introducing a proportional coefficient C, the relationship between ΔP and the equivalent capillary force P_c can be expressed by the following equations:

$$C = \frac{\Delta P}{P_c}, C = \frac{\Delta P_v}{P_c} + 1 \quad (11)$$

According to Equation (11), a proportional coefficient C_0 at the residual state (i.e., at the end of displacement) can be obtained:

$$C_0 = \frac{qL\mu_w M^{1-S_{w\max}}}{kAP_c} + 1 \quad (12)$$

where $S_{w,max}$ is the maximum water saturation at breakthrough under an appropriate displacement rate. Therefore, the coefficient C_0 is undetermined, related to the maximum saturation of displacement, and governs the displacement pattern. Therefore, it can be concluded from Equations (11) and (12) that (1) when $C < 1$, the displacement process is dominated by invasion percolation (capillary fingering); (2) when $C > 1$, the displacement transitions to viscous fingering; and (3) $C = 1$ represents the critical threshold between capillary fingering and viscous flow. To ensure stable viscous flow ($C > 1$), the value of C must be slightly greater than one. Furthermore, the parameter C must meet the following criteria: (1) $C > 1$, indicating the occurrence of viscous flow, based on Section 2.4, C should not be excessively large in order to avoid strong viscous fingering, which can be mitigated by capillary forces; (2) when $C = 2$, the viscous pressure drop ΔP_v approaches the capillary force P_c ($\Delta P_v \approx P_c$), representing the upper limit where capillary forces can suppress the displacement front of viscous fingering. Thus, the displacement condition ($\Delta P > P_c$ and $\Delta P_v \leq P_c$) determines that C_0 should range between 1 and 2.

We calculated the absolute value of C_0 using dynamic network modeling (a $25 \times 25 \times 25$ network) under specific pore-scale heterogeneity ($\sigma/\langle r \rangle = 1.05$, $z = 4$). For a critical capillary number $Ca_c^* \approx 9.56 \times 10^{-6}$, an unfavorable viscosity ratio $M = 100$, and breakthrough water saturation $S_{w,max}$ (approximately 21.8%), the numerical evidence (Figure 4) supports the calculation of C_0 as approximately 1.95, which lies within the reasonable range of one to two. The ratio $\Delta P/P_c \approx 1.98$ ($\Delta P_v \approx 0.98 \times P_c$) indicates that, to achieve a relatively high sweep efficiency in displacements with unfavorable viscosity ratios, the displacement pressure must slightly exceed capillary forces, while the viscous forces should closely approach the capillary forces.

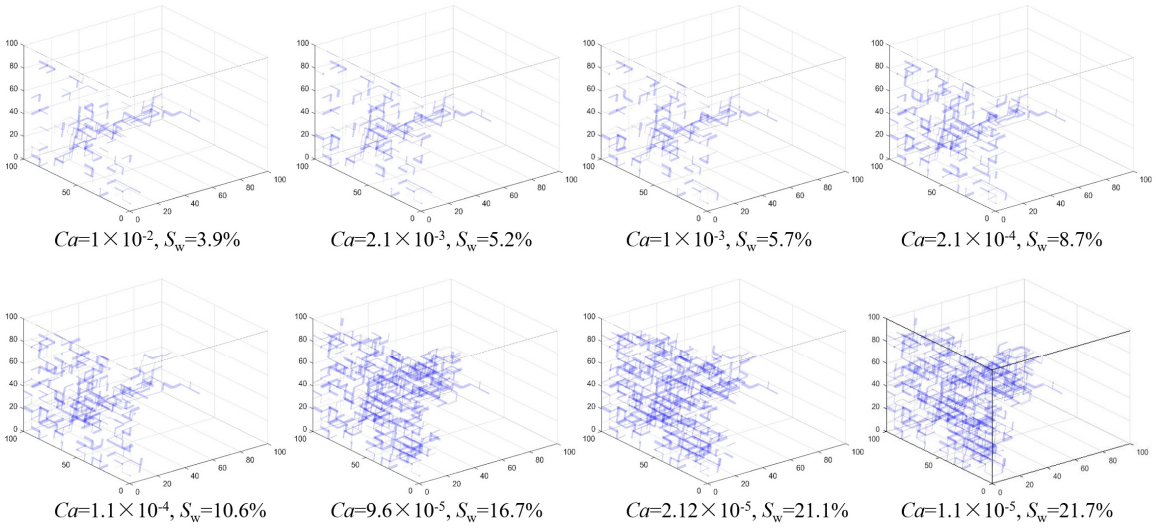


Figure 4. Displacement simulation results in the specific heterogeneous network ($\sigma/\langle r \rangle = 1.05$, $z = 4$) with different capillary numbers, Ca, and the same viscosity ratio ($M = 100$).

On the basis of Equations (7)–(12), we propose a theoretical model for characterizing the transition from strong viscous fingering to relatively stable displacement, influenced by flow rate (critical capillary number Ca_c) and the critical pore throat radius r_c:

$$Ca_c = C_0 \cdot \frac{2\gamma}{r_c \Delta P} \tag{13}$$

where Ca_c is the critical capillary number required to attain $S_{w,max}$ at breakthrough, and C_0 is approximately 1.98. It is worth noting that C_0 = 1.98 is a representative value obtained via fitting/calibration under the baseline network topology, wettability, and parameter range considered in this study, and this value may vary with changes in heterogeneity strength, *Ca*, *M*, and wettability.

Dynamic network simulations (25 × 25 × 25 network) were conducted to investigate the relationship between the capillary number (*Ca*) and water saturation at breakthrough (S_w) under varying pore-scale heterogeneities. The simulation results, summarized in Table 2, provide critical values of the capillary number at breakthrough (Ca_c), maximum water saturation ($S_{w,max}$), and the fitted coefficient (C_0) under different conditions, including variations in *Ca*, viscosity ratio (*M*), and pore-scale heterogeneity parameters (r_c/r_H and σ/<*r*>). The fitted C_0 values range between 1.7 and 2.3, which are in excellent agreement with the theoretical analysis presented earlier, confirming the reliability of the theoretical framework.

Table 2. The values of simulated Ca_c, C_0, and S_{wmax} for different viscosity ratios *M* and different pore-scale heterogeneities.

M	σ/<*r*>	*z*	Simulated Ca_c	S_{wmax}	r_c/r_H	C_0-1
100	0.8	8	2.88×10^{-4}	0.185	0.937409	1.884456
100	0.8	7.2	2.16×10^{-4}	0.194	0.748536	1.715023
100	0.8	6.4	1.59×10^{-4}	0.193	0.884586	1.915587
100	0.8	5.6	1.11×10^{-4}	0.195	0.69584	1.826729
100	0.8	4.8	7.23×10^{-5}	0.239	0.595928	1.862874
100	0.8	4	4.24×10^{-5}	0.245	0.524854	1.916
100	1.05	8	1.01×10^{-4}	0.197	0.921006	1.79465
100	1.05	7.2	9.57×10^{-5}	0.201	0.717649	1.875638
100	1.05	6.4	7.21×10^{-5}	0.253	0.656538	1.951672
100	1.05	5.6	3.60×10^{-5}	0.274	0.557231	1.877533
100	1.05	4.8	2.16×10^{-5}	0.279	0.436147	1.755594
100	1.05	4	9.56×10^{-6}	0.341	0.436584	1.98653
50	0.8	8	5.05×10^{-4}	0.161	0.937409	1.917423
50	0.8	7.2	3.60×10^{-4}	0.176	0.748536	1.804259
50	0.8	6.4	2.55×10^{-4}	0.195	0.884586	1.906172
50	0.8	5.6	1.55×10^{-4}	0.202	0.69584	1.721324
50	0.8	4.8	1.05×10^{-4}	0.226	0.595928	1.764404
50	0.8	4	7.44×10^{-5}	0.267	0.524854	1.990605
50	1.05	8	2.02×10^{-4}	0.229	0.921006	1.968591
50	1.05	7.2	1.36×10^{-4}	0.275	0.717649	1.752565
50	1.05	6.4	1.15×10^{-4}	0.234	0.656538	1.924008
50	1.05	5.6	1.07×10^{-4}	0.229	0.557231	2.25443
50	1.05	4.8	4.25×10^{-5}	0.285	0.436147	1.848304
50	1.05	4	1.19×10^{-5}	0.375	0.436584	1.70544

Figure 5 shows the relationship between capillary number (*Ca*) and water saturation (S_w) at breakthrough. Lower flow rates yield higher invading-phase saturation at breakthrough and more strongly suppress viscous fingering. This indicates that, in CO_2 ge-

ological storage and oil and gas recovery, appropriately reducing the flow rate can improve ultimate recovery and economic performance. The simulations also show that pore-scale heterogeneities strongly affect displacement behavior, highlighting their importance for accurate prediction. Overall, the results confirm the theoretical model and emphasize the roles of capillary number and wettability in controlling displacement pattern transitions.

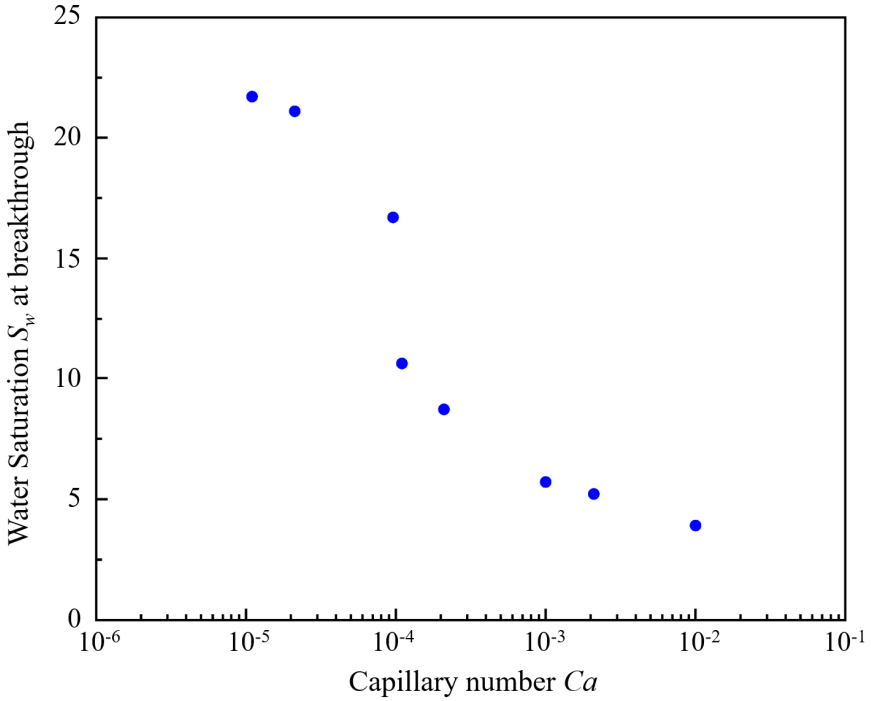


Figure 5. The relation between capillary number *Ca* and water saturation S_w at breakthrough.

In view of the long-standing and widely concerning issue of flow instabilities during immiscible displacement, extensive studies have been conducted at different scales using a variety of methods. Overall, related research has mainly been carried out at two scales: at the reservoir scale, the focus is on production dynamics, flow characteristics, and optimization of development strategies; at the core and pore scales, attention is directed to two-phase flow, capillary effects, and the dominant factors controlling invasion [34]. In addition, the effects of the injection viscosity ratio [35], film flow, and wettability [26] are also highly significant, but this study did not systematically investigate these factors, and these will be a focus of our future work. In terms of pore-scale flow simulations, numerous studies have systematically investigated fingering, channeling, and sweep efficiency during immiscible displacement using interface-tracking/capturing computational fluid dynamics (CFD) methods [36], smoothed particle hydrodynamics (SPHs) [37], pore-network models (PNMs) [12], and lattice Boltzmann methods (LBMs) [38], among others. These methods typically discretize the pore space into small cells or lattices and solve the Navier–Stokes or Boltzmann equations to obtain detailed flow information at the pore–throat scale. However, as the model size increases, the number of cells grows rapidly [39], and the computational cost and memory requirements increase dramatically, posing substantial challenges for engineering applications [35]. In contrast, the present study captures flow instabilities and fingering patterns at a reasonable computational cost, and elucidates, from different perspectives, the formation mechanisms of unstable phenomena such as flow channeling and viscous fingering in immiscible displacement.

Compared with studies based solely on Hele-Shaw systems, the *rc*-*Ca* theoretical framework proposed in this work will provide a valuable complement to the design

and optimization of these time-dependent control strategies in three-dimensional porous media. In addition, the pore-network model in this work assumes "piston-like" pore filling. When the wettability contrast is moderate, the effects of interface snap-off and persistent film flow are relatively weak, and the assumptions of piston-like filling and at most one interface per tube are reasonable. However, for very small pore sizes, strong wettability contrast, or very high viscosity ratios, snap-off events and film flows can become important. In such cases, our model may underestimate the diversity of flow pathways, leading to biased low estimates of *rc*-*Ca*. In addition, the study by Yang et al. [12] shows that compressibility can, to some extent, alter the water saturation at breakthrough, but this influence is not substantial, again primarily because of the limited study scale; at larger scales, compressibility is expected to exert a more pronounced effect on water saturation at breakthrough. Meanwhile, building on the present work, it would be even more valuable to further extend the analysis to the flow of shear-thickening, yield-stress, and power-law fluids [40] in complex and confined geometries, particularly studies that focus on flow stability, fingering behavior, and heat management in channels and porous structures [41]—topics that are directly relevant to the future work envisaged in this paper.

4. Conclusions

This study integrates a three-dimensional BCC pore network with an unsteady-state displacement algorithm to investigate flow channeling and viscous fingering in porous media. The results show that channeling pathways strongly correlate with fingering growth under specific pore–throat structures, consistent with the minimum energy dissipation principle. Fingering evolution is governed by viscous–capillary competition along preferential flow paths, and lowering the injection rate effectively suppresses fingering during immiscible displacement. A unified theoretical model is further proposed to quantify the combined effects of viscous–capillary competition and pore-scale heterogeneity, providing a predictive framework for displacement-front evolution and guidance for optimizing CO_2 injection and improving hydrocarbon recovery.

Author Contributions: Conceptualization, X.Y., B.K. and Y.T.; methodology, X.Y.; software, B.K.; validation, X.Y., B.K. and Q.D.; formal analysis, Z.M.; investigation, C.D.; resources, W.W.; data curation, Q.D.; writing—original draft preparation, X.Y.; writing—review and editing, Y.T.; visualization, B.K.; supervision, Y.T.; project administration, Y.T.; funding acquisition, Y.T. All authors have read and agreed to the published version of the manuscript.

Funding: This research was funded by the National Natural Science Foundation for Youth Grant, grant number 41902157.

Data Availability Statement: The original contributions presented in this study are included in the article. Further inquiries can be directed to the corresponding author(s).

Acknowledgments: We sincerely thank each anonymous reviewer for their helpful suggestions.

Conflicts of Interest: The authors declare no conflicts of interest. Authors Xin Yang, Bo Kang, Qi Deng, Zhongrong Mi and Ce Duan were employed by the Chengdu Northern Petroleum Exploration and Development Technology Co., Ltd. Authors Weiguang Wang and Bo Kang were employed by the EBS Petroleum Co., Ltd. The remaining authors declare that the research was conducted in the absence of any commercial or financial relationships that could be construed as a potential conflict of interest. The Chengdu Northern Petroleum Exploration and Development Technology Co., Ltd. and EBS Petroleum Co., Ltd. had no role in the design of the study; in the collection, analyses, or interpretation of data; in the writing of the manuscript, or in the decision to publish the results.

References

1. Yang, X.; Li, X.; Kang, B.; Xu, B.; Wang, H.; Zhao, X.; Tang, Y. Quantifying the crossover from capillary fingering to viscous fingering in heterogeneous porous media. *Energy Geosci.* **2025**, *6*, 100362. [CrossRef]
2. Blunt, M.; King, P. Scaling structure of viscous fingering. *Phys. Rev. A* **1988**, *37*, 3935. [CrossRef]
3. Regaieg, M.; Moncorgé, A. Adaptive dynamic/quasi-static pore network model for efficient multiphase flow simulation. *Comput. Geosci.* **2017**, *21*, 795–806. [CrossRef]
4. Huang, X.; Bandilla, K.W.; Celia, M.A. Multi-physics pore-network modeling of two-phase shale matrix flows. *Transp. Porous Media* **2016**, *111*, 123–141. [CrossRef]
5. Holtzman, R.; Segre, E. Wettability stabilizes fluid invasion into porous media via nonlocal, cooperative pore filling. *Phys. Rev. Lett.* **2015**, *115*, 164501. [CrossRef]
6. Thepsaskul, W.; Wongsapai, W.; Jaitiang, T.; Jaekhajad, P. Prospects of attaining Thailand's carbon neutrality target through carbon capture and storage by public power utility. *Sustainability* **2025**, *17*, 276. [CrossRef]
7. Zhao, L.; Zhao, Y.; Song, X.; Wang, Y.; Chen, Y.; Zhu, Z.; Geng, J. An experimental study of the elastic properties of the sandstone flooded with supercritical CO_2: The influences of saturation, pressure and temperature. *Geophys. J. Int.* **2025**, *241*, 702–714. [CrossRef]
8. Dias, E.O.; Alvarez-Lacalle, E.; Carvalho, M.S.; Miranda, J.A. Minimization of viscous fluid fingering: A variational scheme for optimal flow rates. *Phys. Rev. Lett.* **2012**, *109*, 144502. [CrossRef] [PubMed]
9. Lenormand, R.; Touboul, E.; Zarcone, C. Numerical models and experiments on immiscible displacements in porous media. *J. Fluid Mech.* **1988**, *189*, 165–187. [CrossRef]
10. Lan, T.; Hu, R.; Yang, Z.; Wu, D.S.; Chen, Y.F. Transitions of fluid invasion patterns in porous media. *Geophys. Res. Lett.* **2020**, *47*, e2020GL089682. [CrossRef]
11. Xu, W.; Ok, J.T.; Xiao, F.; Neeves, K.B.; Yin, X. Effect of pore geometry and interfacial tension on water-oil displacement efficiency in oil-wet microfluidic porous media analogs. *Phys. Fluids* **2014**, *26*, 093102. [CrossRef]
12. Yang, X.; Li, X.; Tang, Y.; Li, M.; Bernabé, Y.; Li, C.; Du, X. Study on non-Newtonian fluid displacement patterns based on the pore network model. *Chin. J. Geophys.* **2023**, *66*, 5157–5172. [CrossRef]
13. Yang, J.; Bondino, I.; Regaieg, M.; Moncorgé, A. Pore to pore validation of pore network modelling against micromodel experiment results. *Comput. Geosci.* **2017**, *21*, 849–862. [CrossRef]
14. Bernabé, Y.; Li, M.; Maineult, A. Permeability and pore connectivity: A new model based on network simulations. *J. Geophys. Res. Solid Earth* **2010**, *115*, B10203. [CrossRef]
15. Talon, L.; Hennig, A.A.; Hansen, A.; Rosso, A. Influence of the imposed flow rate boundary condition on the flow of Bingham fluid in porous media. *Phys. Rev. Fluids* **2024**, *9*, 063302. [CrossRef]
16. Tang, Y.B.; Li, M.; Bernabé, Y.; Zhao, J.Z. Viscous fingering and preferential flow paths in heterogeneous porous media. *J. Geophys. Res. Solid Earth* **2020**, *125*, e2019JB019306. [CrossRef]
17. Razmavar, I.; Alami, F.M.; Rasaei, M.R.; Nadafpour, M. Microscopic fractal-dimension study of rate and viscosity changes on displacement pattern by use of 2D glass micromodel. *SPE Reserv. Eval. Eng.* **2017**, *20*, 8–18. [CrossRef]
18. Al-Housseiny, T.T.; Tsai, P.A.; Stone, H.A. Control of interfacial instabilities using flow geometry. *Nat. Phys.* **2012**, *8*, 747–750. [CrossRef]
19. Liu, H.; Zhang, Y.; Valocchi, A.J. Lattice Boltzmann simulation of immiscible fluid displacement in porous media: Homogeneous versus heterogeneous pore network. *Phys. Fluids* **2015**, *27*, 052103. [CrossRef]
20. Beteta, A.; Sorbie, K.S.; McIver, K. Experimental observations and modeling of the effect of wettability on immiscible viscous fingers at the Darcy scale. *Phys. Fluids* **2024**, *36*, 044111. [CrossRef]
21. Sahimi, M. *Flow and Transport in Porous Media and Fractured Rock: From Classical Methods to Modern Approaches*; John Wiley & Sons: Hoboken, NJ, USA, 2011. [CrossRef]
22. Li, M.; Tang, Y.; Bernabé, Y.; Zhao, J.Z.; Li, X.F.; Bai, X.Y.; Zhang, L.H. Pore connectivity, electrical conductivity, and partial water saturation: Network simulations. *J. Geophys. Res. Solid Earth* **2015**, *120*, 4055–4068. [CrossRef]
23. Chen, M.; Dai, J.; Liu, X.; Kuang, Y.; Wang, Z.; Gou, S.; Li, M. Effect of displacement rates on fluid distributions and dynamics during water flooding in tight oil sandstone cores from nuclear magnetic resonance (NMR). *J. Pet. Sci. Eng.* **2020**, *184*, 106588. [CrossRef]
24. Sogbedji, J.M.; van Es, H.M.; Melkonian, J.J.; Schindelbeck, R.R. Evaluation of the PNM model for simulating drain flow nitrate-N concentration under manure-fertilized maize. *Plant Soil* **2006**, *282*, 343–360. [CrossRef]
25. Adabag, E.; Atal, M.; Gerard, W.; Plancher, B. Mpcgpu: Real-time nonlinear model predictive control through preconditioned conjugate gradient on the gpu. In Proceedings of the 2024 IEEE International Conference on Robotics and Automation (ICRA), Yokohama, Japan, 13–17 May 2024; pp. 9787–9794. [CrossRef]
26. Zhao, B.; MacMinn, C.W.; Juanes, R. Wettability control on multiphase flow in patterned microfluidics. *Proc. Natl. Acad. Sci. USA* **2016**, *113*, 10251–10256. [CrossRef]

27. Sheng, Q.; Thompson, K. A unified pore-network algorithm for dynamic two-phase flow. *Adv. Water Resour.* **2016**, *95*, 92–108. [CrossRef]
28. Aker, E.; Måløy, K.J.; Hansen, A. Simulating temporal evolution of pressure in two-phase flow in porous media. *Phys. Rev. E* **1998**, *58*, 2217. [CrossRef]
29. Fujii, A.; Tanaka, T.; Nakajima, K. Light Weight Coarse Grid Aggregation for Smoothed Aggregation Algebraic Multigrid Solver. *IEEE Access* **2024**, *12*, 57345–57355. [CrossRef]
30. Zheng, Z.; Kim, H.; Stone, H.A. Controlling viscous fingering using time-dependent strategies. *Phys. Rev. Lett.* **2015**, *115*, 174501. [CrossRef]
31. Bernabé, Y.; Bruderer, C. Effect of the variance of pore size distribution on the transport properties of heterogeneous networks. *J. Geophys. Res. Solid Earth* **1998**, *103*, 513–525. [CrossRef]
32. Le Goc, R.; De Dreuzy, J.R.; Davy, P. Statistical characteristics of flow as indicators of channeling in heterogeneous porous and fractured media. *Adv. Water Resour.* **2010**, *33*, 257–269. [CrossRef]
33. Martins, E.Q.; Pascoal, M.M. A new implementation of Yen's ranking loopless paths algorithm. *Q. J. Belg. Fr. Ital. Oper. Res. Soc.* **2003**, *1*, 121–133. [CrossRef]
34. Amirsardari, M.; Afsari, K. Pore-to-field scale modeling of residual gas trapping in tight carbonate underground gas reservoirs. *Energy* **2024**, *298*, 131305. [CrossRef]
35. Yang, Z.; Méheust, Y.; Neuweiler, I.; Hu, R.; Niemi, A.; Chen, Y.F. Modeling immiscible two-phase flow in rough fractures from capillary to viscous fingering. *Water Resour. Res.* **2019**, *55*, 2033–2056. [CrossRef]
36. Basirat, F.; Yang, Z.; Niemi, A. Pore-scale modeling of wettability effects on CO_2–brine displacement during geological storage. *Adv. Water Resour.* **2017**, *109*, 181–195. [CrossRef]
37. Tartakovsky, A.M.; Meakin, P. Simulation of unsaturated flow in complex fractures using smoothed particle hydrodynamics. *Vadose Zone J.* **2005**, *4*, 848–855. [CrossRef]
38. Dou, Z.; Zhou, Z.; Sleep, B.E. Influence of wettability on interfacial area during immiscible liquid invasion into a 3D self-affine rough fracture: Lattice Boltzmann simulations. *Adv. Water Resour.* **2013**, *61*, 1–11. [CrossRef]
39. Sinha, S.; Gjennestad, M.A.; Vassvik, M.; Hansen, A. Fluid meniscus algorithms for dynamic pore-network modeling of immiscible two-phase flow in porous media. *Front. Phys.* **2021**, *8*, 548497. [CrossRef]
40. Garg, A.; Fontana, J.V. Capillary flow dynamics of power-law fluids in root-like networks: Effects of gravity, rheology, and structural complexity. *ChemRxiv* **2025**. [CrossRef]
41. Garg, A.; Akkinepally, B.; Sarkar, J.; Pattanayek, S.K. Emerging perspectives in non-Newtonian fluid dynamics: Research gaps, evolving methods, and conceptual limitations. *Phys. Fluids* **2025**, *37*, 071401. [CrossRef]

Disclaimer/Publisher's Note: The statements, opinions and data contained in all publications are solely those of the individual author(s) and contributor(s) and not of MDPI and/or the editor(s). MDPI and/or the editor(s) disclaim responsibility for any injury to people or property resulting from any ideas, methods, instructions or products referred to in the content.